Matter

Article

Stereoregular self-assembly of biobased recyclable polymer membranes for enantioselective nanofiltration

Graphical abstract

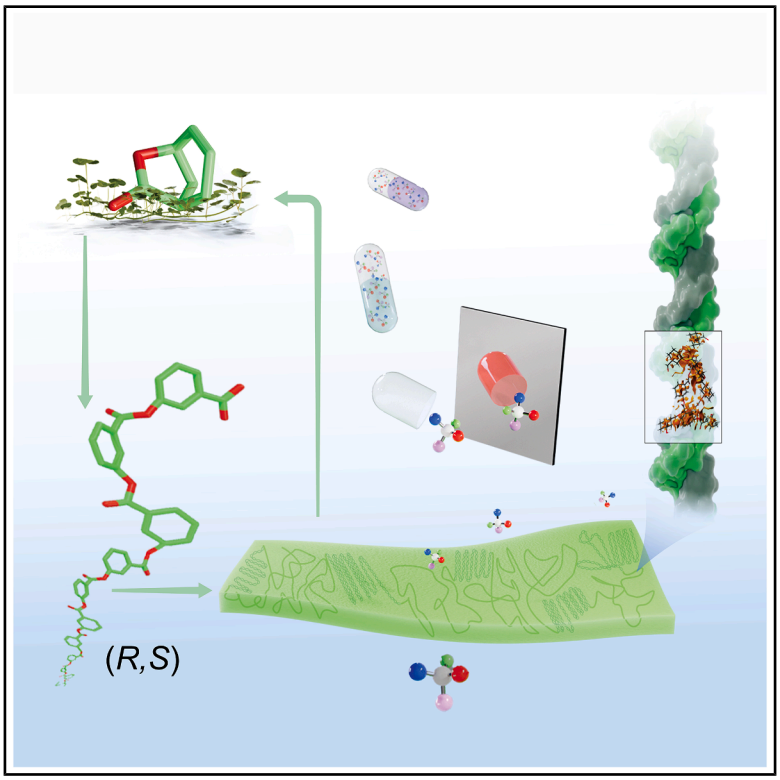

Authors

Diana G. Oldal, Rifan Hardian, Hakkim Vovusha, ..., Changxia Shi, Eugene Y.-X. Chen, Gyorgy Szekely

Correspondence

gyorgy.szekely@kaust.edu.sa

In brief

An intrinsically chiral, biobased polymer with dual stereogenic centers self-assembles into a tightly packed membrane, enabling enantioselective and robust nanofiltration performance without added chiral selectors. Quantifying the permeate and retentate revealed how pressure tunes enantioselectivity and enantiomer rejection, establishing stereoregular self-assembly as a design route to sustainable chiral separations.

Highlights

- Biobased recyclable polyesters with two inherent stereogenic centers are engineered
- Stereoregular self-assembly yielded high-performance polyester membranes
- Dual-function chiral membrane for enantioselective and controllable nanofiltration performance
- Enantiomer selectivity-rejection correlation reveals chiral discrimination mechanism

Oldal et al., 2026, Matter 9, 102797
July 1, 2026
https://doi.org/10.1016/j.matt.2026.102797

2 **Benchmark**
First qualification/assessment of material properties and/or performance

CellPress

Please cite this article in press as: Oldal et al., Stereoregular self-assembly of biobased recyclable polymer membranes for enantioselective nanofiltration, Matter (2026), https://doi.org/10.1016/j.matt.2026.102797

Matter

CellPress

Article

Stereoregular self-assembly of biobased recyclable polymer membranes for enantioselective nanofiltration

Diana G. Oldal,[1,2] Rifan Hardian,[1] Hakkim Vovusha,[1] Maxim V. Peskov,[3] Udo Schwingenschlögl,[3] Changxia Shi,[4] Eugene Y.-X. Chen,[4] and Gyorgy Szekely[1,2,5,*]

[1]Advanced Membranes and Porous Materials Center, Physical Science and Engineering Division, King Abdullah University of Science and Technology (KAUST), Thuwal 23955-6900, Saudi Arabia

[2]Chemical Engineering Program, Physical Science and Engineering Division, King Abdullah University of Science and Technology (KAUST), Thuwal 23955-6900, Saudi Arabia

[3]Materials Science and Engineering Program, Physical Science and Engineering Division, King Abdullah University of Science and Technology (KAUST), Thuwal 23955-6900, Saudi Arabia

[4]Department of Chemistry, Colorado State University, Fort Collins, CO 80523-1872, USA

[5]Lead contact

*Correspondence: gyorgy.szekely@kaust.edu.sa

https://doi.org/10.1016/j.matt.2026.102797

PROGRESS AND POTENTIAL Numerous pharmaceuticals and agrochemicals are mixtures of mirror-image molecules, where one version is beneficial and the other may be inactive or harmful. Efficiently separating these mixtures remains a great challenge. By engineering the polymer's molecular design, we developed a membrane that differentiates between mirror-image molecules without extra chemicals or complex processes while maintaining high stability. This research presents a sustainable approach using a recyclable polymer that self-assembles into more ordered, chiral structures. This strategy can enhance the safety and affordability of pharmaceuticals and specialized chemicals production. The recyclability and durability of these membranes in harsh environments can reduce the environmental impact of chemical manufacturing. This work establishes a foundation for advanced materials with simple designs that improve availability, simplify infrastructure, and lower the cost of pure chemical manufacturing.

SUMMARY

Separation of racemic mixtures is crucial in pharmaceuticals and agrochemicals, whose enantiomers exhibit distinct pharmacological and biological activities. Herein, we design chiral membranes via stereoregular self-assembly of recyclable polymers for enantioselective nanofiltration. By incorporating two inherent stereogenic centers into the repeating unit, we created well-defined chiral recognition sites for amino acids. As a result of stereoregular self-assembly, the polymer adopted more extended conformations with larger radii of gyration, denser packing, and higher crystallinity, leading to superior thermal, mechanical, and chemical stabilities. The dual stereogenic centers enable tailoring both enantioselectivity and nanofiltration performance. We unveil the relation between enantioselectivity and enantiomer rejection, and reveal the effects of applied pressure on the enantioselectivity in both permeate and retentate, highlighting the pressure-dependent separation behavior. The design of stereoregular self-assembled membranes offers intrinsically ordered architectures, refined molecular selectivity, and precise structural control without complex processing, establishing a new design strategy for sustainable, high-performance separation systems.

INTRODUCTION

Chirality refers to the asymmetric arrangements of different atoms, creating nonoverlapping mirror images (enantiomers) of a compound with a given chemical structure. As the enantiomeric purity of chemical compounds is crucial for the environment and human health, enantioselective purification is widely applied to pharmaceuticals,[1,2] pesticides,[3] food additives,[4] and fragrances.[5,6] Enantiomerically pure compounds are most commonly obtained through natural chiral drug extraction, asymmetric synthesis, and enantiomer separation.[7] Isolation of natural chiral drugs is limited by the availability of natural chiral

Please cite this article in press as: Oldal et al., Stereoregular self-assembly of biobased recyclable polymer membranes for enantioselective nanofiltration, Matter (2026), https://doi.org/10.1016/j.matt.2026.102797

compounds and requires a complex extraction process. Asymmetric synthesis can effectively yield pure enantiomers but is costly and requires a long development time.[8] Among the various enantiomer separation techniques—chiral chromatography,[9] enantioselective crystallization,[10] liquid-liquid extraction,[11] classical resolution,[12] chiral adsorption,[13] and chiral membrane separation[14]—membrane-based separation is advantageous due to low cost, low energy consumption, continuous operation, and facile scale-up.[15]

Enantioselective membranes are selective barriers that preferentially allow one of the enantiomers to permeate due to the formation of diastereomeric complexes. Driven by differences in the Gibbs free energy and stability between an enantiomer and the chiral recognition sites in diastereomeric complexes, the enantiomers migrate through the membrane at different rates.[16] Chiral recognition is mediated by van der Waals forces, hydrogen bonding, hydrophobic effects, Coulombic interactions, and steric effects.[17,18] Binding of chiral polymers to enantiomers is often facilitated by specific interactions between the chiral recognition sites and enantiomers.[15] The enantioselectivity of a membrane can stem either from the intrinsic chiral structure of the polymer[17] or from the chiral selectors incorporated into the membrane.[19]

Many researchers have incorporated chiral selectors such as cyclodextrins,[20,21] amino acids,[22,23] deoxyribonucleic acids,[24] proteins,[25] crown ethers,[26] metal-organic frameworks,[27,28] covalent-organic frameworks,[29,30] and ionic liquids[20,31] into enantioselective membranes. Chiral polymer membranes can also be fabricated by polymerizing chiral monomers or employing inherently chiral polymers. Homochiral polymers are particularly promising for chiral separation due to their easy processability. For instance, Wang et al.[32] embedded graphene oxide nanosheets into homochiral poly(2-oxazoline)-based membranes, achieving a high enantiomeric excess (*ee* = 98.3% ± 1.7%) of *S*-limonene. Homochiral polymers with intrinsic microporosity have also demonstrated notable enantioselectivity, with *ee* values of 53% and 32% for racemic BINOL and mandelic acid, respectively.[33,34] Natural enantiopure polymers such as cellulose,[35] chitosan,[36] sodium alginate,[37] and their alternatives, with a high content of asymmetric carbons on their backbone structures,[38] are emerging materials in chiral separation.

Among polymers, polyesters are sustainable, highly biodegradable alternatives that cover 90% of the biodegradable plastics market.[39] However, the use of chiral polyesters as membrane materials for chiral separation has been rarely reported. Ke et al.[40] covalently bonded chiral cyclodextrins selectors to a commercial cellulose acetate membrane, using trimesoyl chloride as the crosslinking agent, forming a chiral polyester composite membrane. Lu et al.[41] similarly fabricated an enantioselective composite membrane via interfacial polymerization of cyclodextrins with trimesoyl chloride on a cellulose nanofiber layer. Although these approaches have successfully formed chiral polyester membranes, they require complex synthesis steps combining multiple monomers, including toxic materials. Therefore, the efficiency and environmental impacts of these membranes have raised concern.

In this study, we incorporate two distinct stereogenic centers into a biobased monomer. Upon polymerization, these chiral centers direct stereoregular self-assembly into hierarchically chiral structures that was achieved without the use of enantiomer mixtures. Besides simplifying the fabrication process, our strategy mitigates environmental concerns by avoiding the use of toxic monomers. Stereoregular self-assembly of a polymer refers to the formation of an organized structure of polymers with regular stereochemistry that is driven by noncovalent interactions (NCIs) such as hydrogen bonding, van der Waals forces, or electrostatic interactions.[42] Increased stereoregularity in the polymer backbone typically enhances its physical and mechanical properties.[43] The self-assembly of stereoregular polymers regulates chain packing, leading to improved molecular order[44] and thermal and mechanical properties.[45] Consequently, we aim to exploit these advantages and design membranes for enantioselective nanofiltration.

Herein, we strategically engineered novel chiral membranes from recyclable poly(*R,S*)-6-oxabicyclo[3.2.1]octan-7-one (PBiL) polyester featuring two inherent distinct stereogenic centers for enantiomer separation and nanofiltration applications (Figure 1). PBiL polyester is recyclable[46] and derivable from natural materials.[47,48] However, depolymerization of the membrane material may require a prior purification step, which should also be considered when assessing end-of-life processing. The monomer of PBiL, BiL, can be regarded as a hybrid structure of five-membered γ-butyrolactone and seven-membered ε-caprolactone. γ-Butyrolactone, a biomass-derived monomer obtained from natural succinic acid, is ranked among the top 12 biomass-derived compounds for petrochemical replacement by the US Department of Energy.[49] ε-Caprolactone, a cyclic ester used in biodegradable polycaprolactone production,[50] can be obtained through microbial oxidation of cyclohexanol into adipic acid.[51] Integrating various analytical techniques with computational simulations, we elucidated the structural features of the polymers and investigated the effects of structural configuration—linear versus cyclic architectures and chiral versus racemic conformations—on membrane performance. Furthermore, we established the interplay between enantioselectivity, enantiomer rejection, and applied pressure, offering insights into the underlying mechanisms of chiral discrimination. Our study elucidates the structure, mechanism, and performance of self-assembled stereoregular polyester membranes, highlighting their promise as advanced materials for sustainable separation technologies.

RESULTS AND DISCUSSION

Rational design of biobased chiral polyesters and membrane formation

To elucidate the effects of stereogenic centers and polymer configurations on the properties of stereoregular polymer membranes, we engineered a series of PBiL polyesters with diverse structural features: chiral versus racemic conformations and linear versus cyclic architectures (Figure S1). The designations and characteristics of the polymers are presented in Table 1. The linear chiral polymer (LCP) and cyclic chiral polymer (CCP) were obtained in their enantiopure and racemic forms, as confirmed by circular dichroism (CD) spectroscopy (Figure 2A).

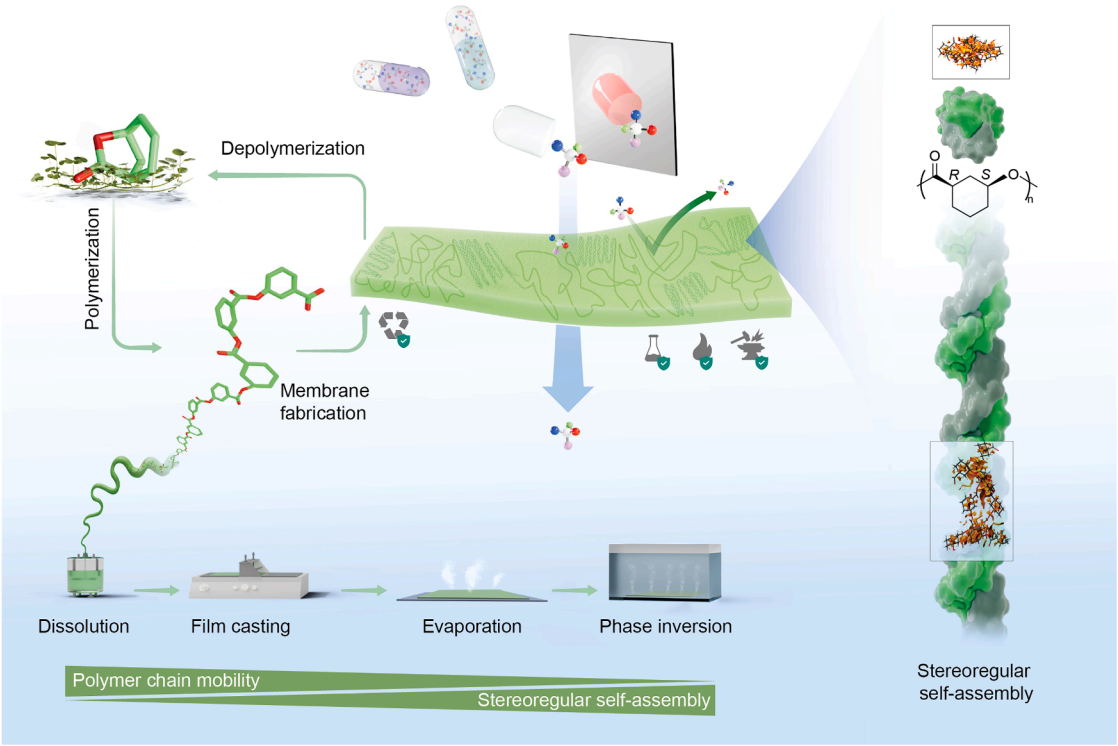

Figure 1. Self-assembled stereoregular membrane design for enantioseparation

The BiL monomer was synthesized from biomass-derived precursors. The PBiL polyester was obtained via ring-opening polymerization of the BiL monomer, using benzyl alcohol as the initiator and La-N as the catalyst in toluene at 23°C. The resulting PBiL was dissolved in dichloromethane (DCM) and processed into membranes through solution casting, followed by 1 min of solvent evaporation and phase inversion in ethanol. The poly(*R,S*)-6-oxabicyclo[3.2.1]octan-7-one (PBiL) monomer could be recovered through catalytic depolymerization. The two inherent stereogenic centers of the polymer promote stereoregular self-assembly. The molecular order was improved by increasing the polymer concentration, thus reducing the polymer chain mobility. The membranes exhibited high chemical, thermal, and mechanical stability, along with selective enantioseparation capabilities.

The pronounced negative and positive bands at 290 and 345 nm, respectively, in the CD spectrum of the LCP indicate a strong interaction between this polymer and circularly polarized light, suggesting the presence of multiple chiral chromophores.[52] Corroborating this observation, the nuclear magnetic resonance (NMR) analysis revealed two chiral centers in the polymer (Figures 2B, S2, S3, S4, and S5). In contrast, the CD spectrum (Figure 2A) of the CCP showed no obvious peaks, suggesting that the interaction between circularly polarized light and the cyclic structure was disrupted, leading to signal interference or suppression. The signal between 270 and 310 nm likely manifests from transition of the carbonyl chromophore at 280 nm.[53] Given the absence of an extended conjugated system, the signal at 345 nm may result from a specific electronic transition influenced by the molecular environment. Overall, the CD spectra confirm the chirality of both the LCP and CCP. In contrast, the CD spectra of the other two polyesters—the linear racemic polyester (LRP) and cyclic racemic polyester (CRP)—showed no signal, confirming their racemic nature.

To further clarify the chirality, we measured the optical rotations of the polymers. The specific rotations of LCP and LRP were $[\alpha]_{589}^{21.7}$ = 64 ° dm^{-1} g^{-1} cm^{-3} and $[\alpha]_{589}^{21.9}$ = 15 ° dm^{-1} g^{-1} cm^{-3}, respectively, whereas those of CCP and CRP were $[\alpha]_{589}^{21.4}$ = 58 ° dm^{-1} g^{-1} cm^{-3} and $[\alpha]_{589}^{21.9}$ = 4 ° dm^{-1} g^{-1} cm^{-3}, respectively. The higher optical rotation values of LCP and CCP than of their racemic counterparts confirm their chiral nature. As the molecular weight of a polymer can affect the enantioselectivity[54–56] and the nanofiltration performance,[57] it is important to address the exact molecular weight for reproducibility. The LCP exhibited a lower number-average molecular weight (M_n = 31.5 kDa) and broader dispersity ($Đ$ = 1.90) (Figure S6A) than LRP (M_n = 78.5 kDa; $Đ$ = 1.32; Figure S6B). The M_n and $Đ$ of CCP/CRP were 8.2/37.1 kDa and 1.63/16.1, respectively (Figures S6C and S6D).

Polymers are preprocessed by dissolution in suitable solvents followed by casting and phase inversion to obtain membranes. After screening of 43 solvents (Table S1), only dichloromethane (DCM) and chloroform were identified as being suitable (Figure S7). DCM was selected for membrane fabrication because it is less toxic than chloroform, as stated in the GlaxoSmithKline solvent-selection guide.[39]

To investigate the effects of DCM on polymer dissolution, we estimated the polymer-solvent interaction energy through density functional theory (DFT) calculations. The interaction energy

Please cite this article in press as: Oldal et al., Stereoregular self-assembly of biobased recyclable polymer membranes for enantioselective nanofiltration, Matter (2026), https://doi.org/10.1016/j.matt.2026.102797

Table 1. Designations, polymer characteristics, and film-forming abilities of the designed PBiLs

Polymer code	Structural configuration	Structural conformation	M_n (kDa)	$Đ$ (–)	Film forming	Membrane code
LCP	linear	chiral	31.5	1.90	yes	LCM
LRP	linear	racemic	78.5	1.32	yes	LRM
CCP	cyclic	chiral	8.2	1.63	no	n.a.
CRP	cyclic	racemic	37.1	16.10	yes	CRM

n.a., not applicable.

($E_{interaction}$) was considerably higher between DCM and LRP (−9.37 kcal mol^{-1}) than between DCM and LCP (−6.06 kcal mol^{-1}) (Figure 2C), indicating that LRP is more stable than LCP in DCM. This observation is further evidenced by the more negative solvation free energy ($\Delta G_{solvation}$) of LRP in DCM (suggesting a more energetically favorable solvation process) than of LCP in DCM. Aligning with these findings, the experiments revealed that LRP remains fully soluble in DCM at concentrations above 3 wt %, whereas LCP is less soluble at similar concentrations. Owing to its rigid and ordered structure, LCP is less likely to interact favorably with DCM than the more flexible LRP (Figure 2C).

The linear polymers (LCP and LRP) with good film-forming ability were deemed suitable for membrane preparation. In contrast, the CCP did not form a film (Figure S8A), possibly because its molecular weight was too low. Although CRP demonstrated film-forming ability (Figures S8B and S8C), it was excluded because a racemic polymer is unsuitable for chiral separation. Scanning electron microscopy (SEM) images of the membranes fabricated from LCP and LRP, denoted as LCM and LRM, respectively, revealed dense morphologies with similar thicknesses (~7.1 μm; Figures S9D and S9E). The LCM exhibited a more textured surface morphology than the LRM (Figures 2D and 2E). From the atomic force microscopy (AFM) analysis, the root-mean-square roughness values (R_q) of LCM and LRM were determined as 9.7 ± 0.5 and 0.7 ± 0.1 nm, respectively (Figures 2D, 2E, S9D, and S9E), confirming the rougher surface morphology of LCM. Both membranes were hydrophilic (contact angle < 90°) owing to the ester groups in their polymer structures (Figures 2D and 2E).

The X-ray diffraction (XRD) patterns (Figure S9A) of LCM and LRM presented broad peaks indicating the amorphous-dominated structure of both membranes. The membranes yielded slightly sharper XRD peaks than the pristine polymers, suggesting that the polymer chains had become partially rearranged into a more ordered structure during membrane formation. In addition, the diffraction peaks in the patterns of both membranes were systematically shifted toward lower 2θ angles from those of their corresponding polymers. Specifically, the XRD peaks of LCP and LCM at 20.2° and 17.5°, respectively, and peaks at 20.4° and 18.4° appeared in the XRD patterns of LRP and LRM, respectively. This shift to lower diffraction angles implies an increased interchain d-spacing, possibly because the polymer chains were relaxed and reorganized during the casting process.

Stereoregular self-assembly in the polymers and membranes

A heterochiral arrangement of two distinct stereogenic centers per repeating unit can enhance the molecular order of a polymer, in contrast to the homochiral arrangement.[58] The LCP possesses two stereogenic centers with opposite configurations (*R* and *S*, Figure S1), which facilitate stereoselective interactions between the polymer chains and, hence, self-assemble to form tighter chain packing. To investigate the self-assembly of LCP, the stabilization energies were calculated using DFT. The optimized total energies of the LCP and LRP systems were 4.21 and 13.24 kcal mol^{-1}, respectively (Figure 3A), demonstrating the higher stability of the LCP than that of the LRP. The stability of the LCP is attributed to the low energy of the chain conformation, which promotes an ordered chain arrangement. In contrast, the LRP adopts a distorted conformation (Figure 3A) that may hinder the formation of an orderly packed structure. To account for the thermodynamics of stereoregular self-assembly, we formulated a hypothesis based on Flory-Huggins theory (Note S2).[59–61] As each repeating unit in the enantiomerically pure LCP shares the same absolute stereochemistry, two chains can align in a perfect mirror-image fashion, forming a continuous row of C–H···O hydrogen bonds at every backbone repeat as observed in other polyester systems.[62] The mixing free energy (ΔG_{mix}) at the resulting uniform *R*–*S* interface is largely negative, maintaining the blend in a single phase in which total hydrogen-bond stabilization drives the stereoregular self-assembly. In contrast, each repeating unit in the racemic LRP is randomly derived from equal proportions of the two mirror-image monomers, preventing continuous *R*–*S* pairing across an entire chain-chain interface. In LRP, few *R*–*S* contacts tend to align in the correct orientation for C–H···O bonding; the majority of nearest-neighbor encounters involve *R*–*R* or *S*–*S* pairs that provide no extra hydrogen-bond stabilization.[63] Therefore, ΔG_{mix} is positive and far exceeds the crystallization threshold, inducing separation of the material into *R*-rich and *S*-rich domains before crystals can form. Without a continuous *R*-*S* interface, self-assembly cannot occur, and the LRP remains amorphous.

Self-assembly in the LCP and its membrane counterpart (LCM) was compared in molecular dynamics (MD) simulations of their structural configurations. The LCP was modeled in toluene to reflect its polymerization synthesis conditions, whereas the LCM was simulated in DCM to represent the solvent environment of the membrane fabrication. The atomic spatial organizations and intermolecular interactions in DCM and toluene were investigated through a radial distribution function (RDF) analysis and nonbonded energy calculations. The RDF quantifies the likelihood of finding a neighboring atom at a given distance from a reference atom, providing insight into the spatial organization of atoms. Nonbonded energy assessments capture the strength of intermolecular interactions, with more negative energies indicating stronger interactions. The LCM yielded

Please cite this article in press as: Oldal et al., Stereoregular self-assembly of biobased recyclable polymer membranes for enantioselective nanofiltration, Matter (2026), https://doi.org/10.1016/j.matt.2026.102797

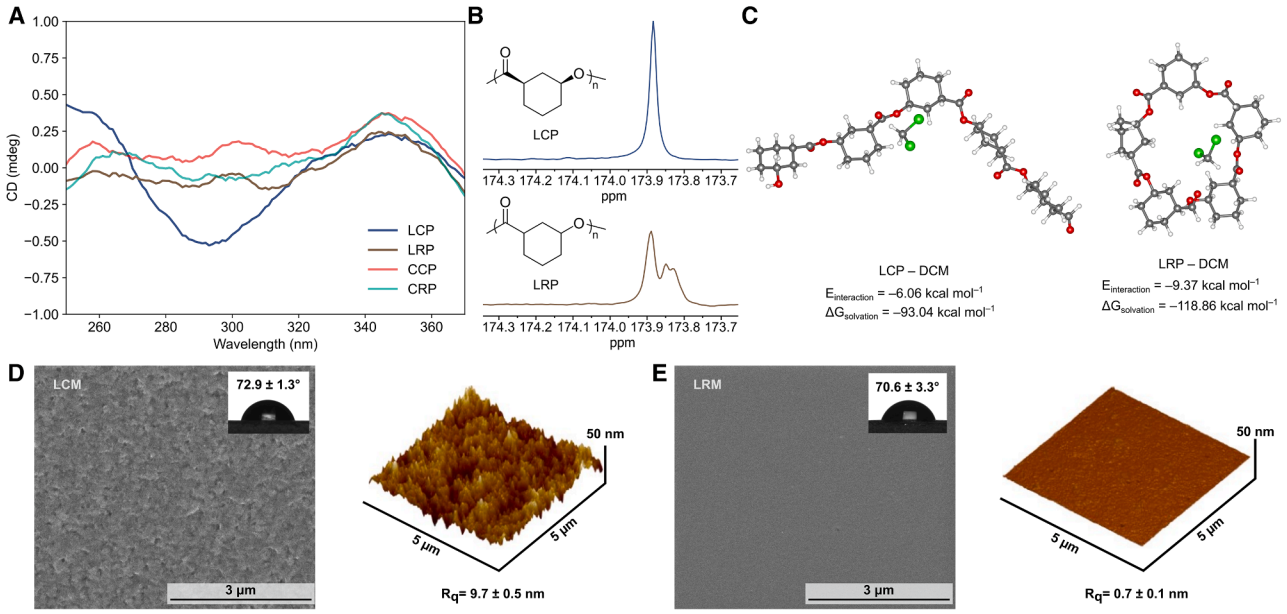

Figure 2. Polymer and membrane properties

(A and B) Circular dichroism (A) and ^{13}C NMR (B) spectra of the different polymers (see Figures S3 and S5 for the full NMR spectra).

(C) Molecular structures optimized in dichloromethane, along with their interaction energies and solvation free energies.

(D and E) Surface scanning electron microscopy (SEM), water contact angle (WCA), and atomic force microscopy (AFM) 3D surface topography images of LCM (D) and LRM (E).

pronounced RDF peaks (Figure 3B), indicating stronger binding interactions and greater entanglement of the polymer chains in LCM than in the LCP. The calculated nonbonded energy (Figure 3C) was substantially higher in LCM (−8,505 kcal mol^{-1}) than in LCP (−7,700 kcal mol^{-1}). Furthermore, the MD snapshots (Figure 3D) revealed that LCM is structurally more compact than LCP, indicating its stronger molecular interactions. Collectively, these findings suggest that the DCM environment strengthens the secondary interactions, creating a more ordered and tightly bound polymer network.

To corroborate the MD simulations results, we measured the characteristic changes in melting temperature arising from adjacent packing of the polymer chains, strong intermolecular interactions, and increased crystallinity. The differential scanning calorimetry (DSC) profile of the LCP (Figure 3E) exhibited a melting temperature (T_m) of 237°C during the first heating cycle, a crystallization peak (T_c) at 223°C during the cooling cycle, and a second melting peak (T_m) at 258°C during the second heating cycle. The distinct melting and crystallization peaks suggest a high-order structure within the chiral structure. The DSC thermogram of LCM (Figure 3F) similarly displayed obvious melting peaks at 266°C and 258°C during the first and second heating cycles, respectively, and a sharp crystallization peak at 225°C. The lower T_m of LCP than of LCM indicates the higher thermal stability of LCM, likely owing to its more ordered structure. Moreover, the melting and crystallization enthalpies were lower in LCP (22.9 and 13.3 J g^{-1}, respectively) than in its membrane counterpart (26.5 and 14.1 J g^{-1}, respectively), indicating a higher crystalline content in LCM than in LCP. According to this observation, the membrane fabrication process facilitates self-assembly, probably by enhancing the secondary intermolecular interactions. The increased structural arrangement resulting from the enhanced molecular ordering is consistent with the XRD results (Figure S9A), which show sharper diffraction peaks for the membranes than for the corresponding polymers. Meanwhile, the DSC profiles of both LRM and LRP only exhibited a glass transition temperature (T_g) during the heating and cooling cycles (Figures 3G and S9C). The absence of detectable T_m and T_c indicates the mostly amorphous nature of these samples. The disordered polymer network in LRP and LRM is attributed to the lack of stereoregularity, which limits the occurrence of secondary interactions.

Furthermore, we hypothesized that increasing the polymer concentration in the membrane enhances molecular ordering by increasing the density of available stereoregular centers. To confirm this hypothesis, we prepared membranes from polymers at three concentrations and obtained their XRD patterns (Figure S10A). As the polymer concentration increased, the diffraction peaks sharpened and the integrated peak area grew, confirming an increasing degree of crystallinity. Corroborating these findings, the T_m in the DSC profile increased with the increasing polymer concentration (Figure S10B and Table S2), indicating a higher degree of molecular ordering in the membranes. Together, these results indicate that increasing the polymer concentrations increases the density of stereoregular interactions, and hence the ordering and crystallinity of the self-assembled membrane.

The crystallinity and long-range structural ordering in the LCM and LRM were investigated using wide-angle X-ray scattering (WAXS). The WAXS scattering patterns of both LRM and LCM

Please cite this article in press as: Oldal et al., Stereoregular self-assembly of biobased recyclable polymer membranes for enantioselective nanofiltration, Matter (2026), https://doi.org/10.1016/j.matt.2026.102797

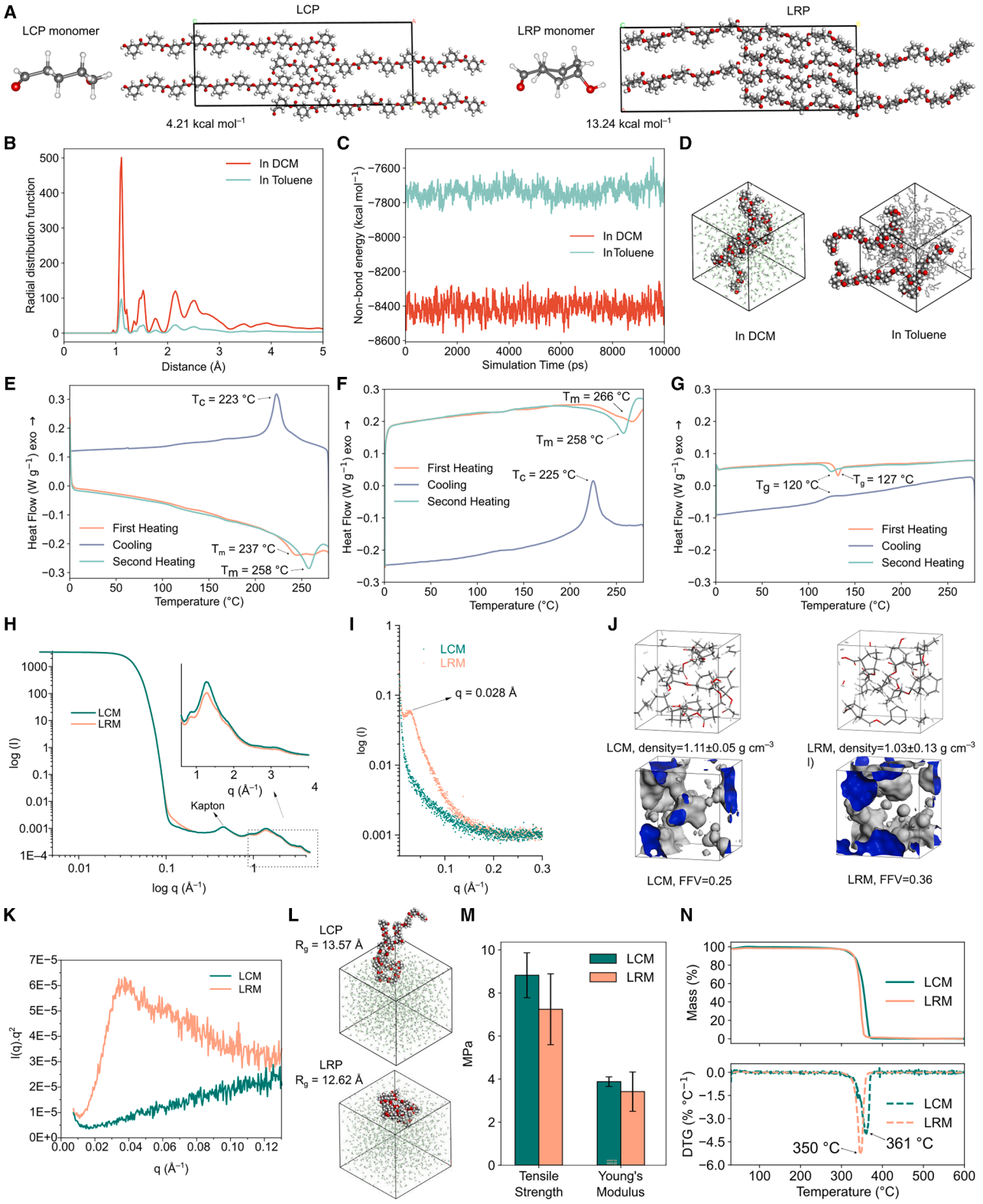

Figure 3. Stereoregular self-assembly

(A) Predicted crystalline structures of the LCP and LRP systems.

(B) Radial distribution functions of the LCP chains in dichloromethane (DCM) and toluene.

(legend continued on next page)

(Figure 3H) were consistent with the degree of structural ordering. The peak at the scattering vector (q) of approximately 0.42 $Å^{-1}$ was assigned to the Kapton tape[64] adhering the membrane samples to the holder. The magnified WAXS spectra of LRM and LCM at higher q values (0.5–4 $Å^{-1}$) were similar, with observable scattering peaks at approximate q values of 0.86 and 1.28 $Å^{-1}$, respectively, and shoulders at 1.84 and 3.21 $Å^{-1}$, respectively. However, as shown in the inset of Figure 3H, the scattering intensity was higher in the WAXS patterns of LCM than in those of LRM, suggesting a higher degree of structural ordering in LCM. These results validate the DSC results.

Figure 3I shows the small-angle X-ray scattering (SAXS) results of the LCM and LRM membranes. The SAXS spectrum of LRM displayed a primary correlation peak at a small scattering vector ($q = 0.028$ $Å^{-1}$), indicating a large average distance ($d = 224$ Å) between the polymer domains[65] and a lower density in LRM than in LCM. To better understand the polymer packing in the membranes, we measured the densities of LCM and LRM (Figure 3J), obtaining 1.11 and 1.03 g cm^{-3}, respectively. The higher density in LCM was attributed to the more compact structure of the chiral polymer and the chirality-driven stereoregular self-assembly, which results in a densely ordered membrane architecture. Consequently, the fractional free volume (FFV) was lower in LCM (0.25) than in LRM (0.36), consistent with the tighter chain packing in LCM (Figure 3A). The packing is then tightened by the large number of intermolecular interactions.

The degree of unfolding in the polymer chains, which correlates with the flexibility of the chains, was qualitatively assessed from Kratky plots derived from the SAXS profiles (Figure 3K). The Kratky plot of the LRM showed a prominent parabolic curve, suggesting a coil arrangement of the polymer chains within a globular shape.[66] Contrarily, the LCM displayed a linearly increasing trend with a less discernible shape, which characterizes unfolded polymer chains. These experimental results agree with the MD-simulated polymer conformation in DCM: LCP exhibited an extended conformation with a gyration radius of 13.57 Å, whereas the LRP showed a coiled conformation with a gyration radius of 12.62 Å (Figure 3L).

The mechanical properties of the chiral and racemic membranes were assessed through a stress-strain analysis (Figure S9B). The Young's modulus was determined from the linear elastic region of the curves, while the tensile strength was obtained from the maximum stress prior to failure. The LCM exhibited a considerably higher Young's modulus and tensile strength than the LRM (Figure 3M and Table S3). We hypothesize that the stereoregular self-assembly in the LCM acts as intermolecular noncovalent crosslinking, which increases the connectivity, reinforcing the structure, and hence enhancing the mechanical properties. These findings are consistent with previous reports demonstrating that, compared to their nonassembled analogues, films that are formed by stereoregular self-assembly exhibit higher tensile strength, increased Young's modulus, and greater elongation at break.[43,67,68]

The LCM and LRM exhibited high thermal stabilities with no signs of degradation up to 340°C (Figure 3N). However, as revealed in the differential thermogravimetric (DTG) analysis, the maximum degradation rate is 350°C for LRM and 361°C for LCM, indicating that LCM is more thermally stable than LRM. Therefore, stereoregular self-assembly effectively increases the thermal stability of materials, consistent with literature findings.[67] Integrating the experimental characterizations and computational simulation results, we conclude that stereoregular self-assembly can effectively tune both the structural arrangement and the mechanical and thermal properties of the membranes.

Performances of the chiral polyester membranes

The two stereogenic centers in each repeating unit of the LCP backbone serve as chiral recognition sites, enabling stereoregular self-assembly into a densely ordered LCM structure that establishes a chiral environment for enantiomer discrimination. Chiral selectivity is quantified as the ratio of retention times of the two enantiomers retained by the membranes. To investigate the chiral separation of various racemic solutes, we calculated the atomic distances between the polymer and racemic solutes through MD simulations (Figure 4A). In all cases, the polymer-solute system dissociated within 30,000 ps, as evidenced by the increasing atom-atom distances between the polymer and solute (Figures S14, S16, S17, and S18). Based on the estimated retention times, the chiral selectivity was maximized in mandelic acid. Consequently, we examined the NCIs between the enantiomers of mandelic acid and the chiral membrane. The dense green regions in the NCI plots (Figure 4B) reveal stronger binding of *D*-mandelic acid than of *L*-mandelic acid to the chiral membrane (Table S4), reflecting enhanced van der Waals interactions and greater spatial complementarity between *D*-mandelic acid and the chiral membrane. In contrast, green surfaces in the NCI plot of *L*-mandelic acid are less intense and more extended, suggesting less favorable binding of the *L*-enantiomer (Figure 4C).

We also conducted MD simulations of the polymer-solute binding energies (Figure S15 and Table S4). In mandelic acid, phenylalanine, and tryptophan (selected as representative solutes), the retention times were short, moderate, and long, respectively. Binding energy calculations across uniformly

(C) Nonbond energy simulations of the LCP in DCM and toluene.
(D) Molecular dynamics snapshots illustrating the self-assembly of LCP chains in DCM and toluene.
(E–G) Differential scanning calorimetry (DSC) thermograms of LCP (E), LCM (F), and LRM (G).
(H and I) Wide-angle X-ray scattering spectra (H) and small-angle X-ray spectra (I) of LCM and LRM.
(J) Molecular simulations and fractional free volumes (FFVs) of LCM and LRM; the gray, red, and white spheres represent C atoms, O atoms, and H atoms, respectively.
(K) Kratky plots of LCM and LRM.
(L) Radii of gyration and conformations of LCP and LRP in DCM.
(M and N) Tensile properties (M) and thermogravimetric analysis (TGA) and differential thermogravimetric (DTG) spectra (N) of LCM and LRM.

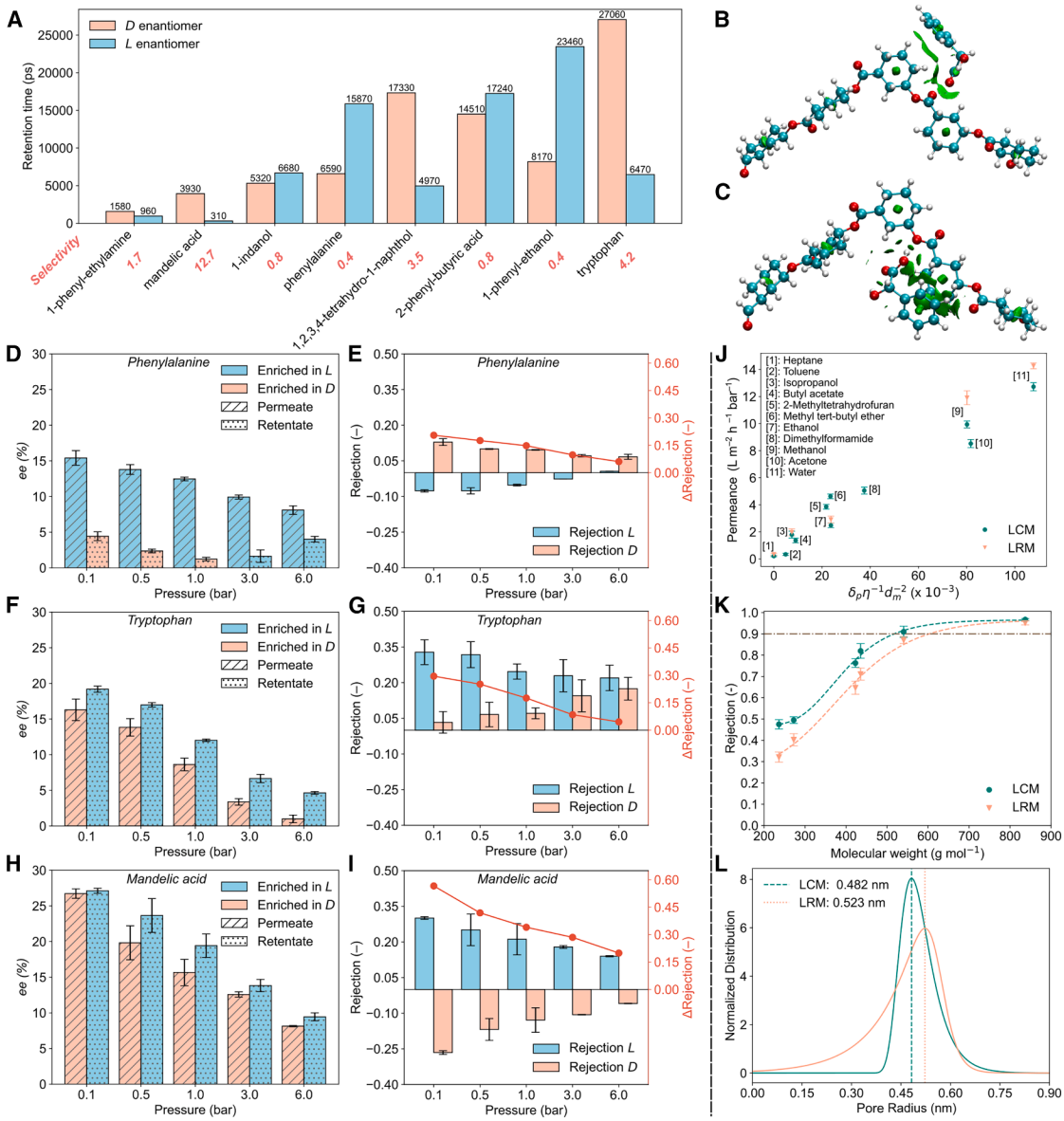

Figure 4. Enantiomer separation and nanofiltration performance

(A) Retention times of solute molecules on the polymer.

(B and C) Noncovalent interactions between the chiral membrane and *D*-mandelic acid (B) and *L*-mandelic acid (C).

(D, F, and H) Enantiomeric excesses of racemic phenylalanine (D), racemic tryptophan (F), and mandelicacid (H) at different transmembrane pressures.

(E, G, and I) Rejection and rejection differences of the two enantiomers of phenylalanine (E), tryptophan (G), and mandelic acid (I) at different transmembrane pressures. The pink and blue bars correspond to the R/D and S/L isomers, respectively.

(J) Solvent permeance as a function of solvent parameters.

(K) Solute rejection in methanol as a function of solvent molecular size.

(L) Pore size distributions of LCM and LRM. The estimated pore sizes of the membranes are given.

spaced frames along the MD trajectories initially fluctuated, then sharply declined as the polymer-solute distance increased (Table S4 and Figure S15). The average polymer-solute binding energies of the *L*- and *D*-enantiomers were positively correlated with their retention times: higher binding energies were associated with longer retention times (Table S4 and Figure 4A). The retention times of isomers (e.g., *L*- and *D*-phenylalanine) are primarily determined by the polymer-solute binding energy. However, according to comparisons of the retention times of different molecules (e.g., mandelic acid, phenylalanine, and tryptophan), the separation of such molecules is influenced by factors other than the binding energy, namely hydrogen bonding, electrostatic and van der Waals forces, the steric-hindrance effect, and other molecular interactions.[69,70]

Please cite this article in press as: Oldal et al., Stereoregular self-assembly of biobased recyclable polymer membranes for enantioselective nanofiltration, Matter (2026), https://doi.org/10.1016/j.matt.2026.102797

The computational predictions were validated through chiral separation experiments on the three selected racemic amino acids. Figure 4D plots the *ee* values of phenylalanine in both the permeate and retentate as the functions of applied pressure. Whereas many studies have reported *ee* only in the permeate,[71,72] we measured both the permeate and retentate to more comprehensively evaluate the separation performance and enantiomeric selectivity under different operating conditions. Aligning with the computational predictions (Figure 4A), *L*-phenylalanine was consistently enriched in the permeate across all tested pressures, reaching a maximum *ee* value of 15.41% ± 1.03% at 0.1 bar. However, the enantioselectivity gradually decreased with further increase in transmembrane pressure. At 6 bar, the *ee* value fell to 8.10% ± 0.6%, nearly half its initial value, indicating that the membrane partially lost its enantiomer-differentiation ability under elevated pressure (Figure 4D). Previous studies have attributed the *ee* decrease to a coupling effect under increasing transmembrane pressure.[73] Increasing the pressure increases the quantity of solute permeating through the membrane, thereby reducing the enantioselectivity. This behavior was explained by the solution-diffusion model, which describes membrane transport as a sequence of sorption, diffusion, and desorption steps. Chiral selectivity arises when each enantiomer interacts differently with the membrane during sorption and diffusion. Under higher pressures, the decreased residence time of the solute within the membrane reduces the likelihood of enantioselective interactions, particularly during diffusion. Additionally, enantioselectivity can be influenced by molecular interactions and its conformational changes (Note S4).[74,75] MD simulations showed the pressure-induced changes in polymer conformation (Figure S19D), where increasing pressure led to chain compaction, as evidenced by a decrease in the radius of gyration. This compaction reduces the accessibility of chiral binding sites, likely contributing to decreased enantioselectivity at higher pressures.

In contrast, the retentate was initially modestly enriched in *D*-phenylalanine at low pressures, but both the permeate and retentate became enriched in the *L*-enantiomer at 3.0 and 6.0 bar, respectively. This behavior can be rationalized by the stronger binding affinity of *L*-phenylalanine (−39.5 kJ mol^{-1}) than of *D*-phenylalanine (−33.2 kJ mol^{-1}) to the chiral membrane (Table S4). At low pressures, this interaction promotes the selective transport of *L*-phenylalanine into the permeate, while retaining some *D*-phenylalanine in the retentate. As the pressure increases, the elevated flux saturates the chiral binding sites faster and reduces the interaction times, resulting in less *L*-phenylalanine being able to pass and thus its greater enrichment in the retentate than in *D*-phenylalanine. More *L*-phenylalanine then passes through the membrane, while its presence in the retentate increases due to incomplete selectivity. This reverse separation behavior at a particular pressure is reflected in the flux-selectivity tradeoff described by the solution-diffusion model.[76] Furthermore, the enantioselectivity of the membrane remained stable, with minimal *ee* variations (Figure S19A) over three separation cycles with phenylalanine, demonstrating promising operational stability and reproducibility.

The enantiomer-rejection profile of phenylalanine (Figure 4E) reveals negative rejection of the *L*-enantiomer from 0.1 to 3 bar, suggesting that the *L*-enantiomer is preferentially transported over the *D*-enantiomer. Negative rejection occurs when one enantiomer has a stronger affinity for the membrane material than for the solvent, resulting in preferential permeation.[77] To rationalize this behavior, the binding energies between the chiral polymer and the phenylalanine enantiomers, as well as between the polymer and solvent, were calculated (Figure S19E). The results indicated that the *L*-enantiomer interacts more strongly with the polymer than with water, which is consistent with its preferential permeation and the observed negative rejection. This interpretation is consistent with the *ee* data shown in Figure 4D. Moreover, the decreasing rejection values of both the *D*- and *L*-enantiomers with increasing pressure limited the interactions between the enantiomers and chiral recognition sites, thereby lowering the enantioselectivity.

The tryptophan permeate (Figure 4F) was enriched in the *D*-enantiomer, with an *ee* of 16.30% ± 1.51% at 0.1 bar. Increasing the pressure decreased the *ee* in the permeate, as observed for phenylalanine. In contrast to phenylalanine, the tryptophan retentate was strongly enriched in *L*-enantiomer (*ee* = 19.19% ± 0.43% at 0.1 bar). Therefore, the enantiomer distribution between the permeate and retentate for tryptophan in the membrane opposed that of phenylalanine, although both solutes exhibited the same trends of *ee* with increasing pressure. Such contrasting enantioseparation behavior between phenylalanine and tryptophan has been reported in other studies.[78,79] Unlike phenylalanine and mandelic acid, tryptophan displayed only positive rejection in its rejection profile (Figure 4G), indicating no preferential transport of either enantiomer. This behavior is attributed to the smaller difference between the polymer-solute binding energies of the tryptophan enantiomers (3.4 kJ mol^{-1}) than between those of phenylalanine (6.3 kJ mol^{-1}) and mandelic acid (4.5 kJ mol^{-1}) (Table S4). As the pressure increased, rejections of the *L*- and *D*-enantiomers of tryptophan decreased and increased, respectively.

Experimentally, the membrane exhibited the highest enantioselectivity for mandelic acid, as predicted in the simulations. Specifically, mandelic acid yielded the highest *ee* values (26.73% ± 0.66% for *D*-mandelic acid in the permeate and 27.12% ± 0.36% for *L*-mandelic acid in the retentate at 0.1 bar) among the tested solutes (Figure 4H). The pressure-dependent trend of mandelic acid followed that of tryptophan (Figure 4F), although with slightly higher *ee* values. Contrary to tryptophan, mandelic acid exhibited negative rejection of its *D*-enantiomer (Figure 4I), likely because the *D*-enantiomer preferentially interacted with the membrane (Figure 4B and Table S4). Although the *ee* values are moderate relative to some membranes that incorporate dedicated chiral selectors (Table S8), the results demonstrate that measurable enantioselectivity is achievable with a single-component, intrinsically chiral polymer membrane in the absence of additional chiral selectors. This finding underscores a balanced design strategy between materials simplicity and membrane performance.

Interestingly, regardless of the rejection direction (positive or negative) and solute, the changes in rejection values ($\Delta_{Rejection}$) with pressure (Figures 4E, 4G, and I) were strongly correlated with the enantioselectivity trends (Figures 4D, 4F, and 4H).

Therefore, the applied pressure plays a crucial role in enantioselectivity; under higher pressures, the rejection difference between enantiomers is minimized, and the chiral separation performance diminishes.

Next, we extended the application of LCM and LRM to aqueous and organic solvent nanofiltration (OSN). The LCM with a higher solvent resistance relative to the LRM (Figure S7 and Table S1) was tested over a wider range of solvents, highlighting its broader chemical compatibility than the LRM, which was limited to only five solvents. The solvent permeance was nearly linearly correlated with the solvent parameters (Figure 4J), which combine the polar contribution of the Hansen solubility parameters (δ_P), inverse viscosity (η), and inverse molar diameter (d_m).[80] The permeances of all tested solvents were lower through LCM than through LRM because the dense molecular configuration of the LCM lowers the FFV, consequently hindering the solvent-molecule transport. Water exhibited the highest permeance (Figure 4J) among the tested solvents (Table S5) owing to its high δ_P value (16 $MPa^{1/2}$), moderate viscosity (1.00 mPa s), and small molar diameter (0.39 nm). The water permeance was slightly lower through the LCM (12.7 ± 0.3 L m^{-2} h^{-1} bar^{-1}) than through the LRM (14.3 ± 0.2 L m^{-2} h^{-1} bar^{-1}). Permeances of the alcohols decreased with the increasing viscosity and molar diameter. The methanol permeance through LCM and LRM was 9.9 ± 0.3 L m^{-2} h^{-1} bar^{-1} and 11.9 ± 0.5 L m^{-2} h^{-1} bar^{-1}, respectively, whereas ethanol showed lower permeance values of 2.5 ± 0.2 L m^{-2} h^{-1} bar^{-1} and 2.9 ± 0.3 L m^{-2} h^{-1} bar^{-1} through LCM and LRM, respectively. Nonpolar solvents such as heptane and toluene, with the lowest δ_P values, exhibited the lowest permeances. Alongside water, acetone (tested only through the LCM) and methanol exhibited high permeances, indicating that both membranes favor the transport of polar solvents with low-to-moderate viscosities and small molar diameters.

To evaluate the solute rejection performances of the membranes in OSN, we prepared feed solutions containing a mixture of six small molecules (molecular weights less than 850 g mol^{-1}; Table S6). Figure 4K plots the solute rejection values of the membranes as functions of molecular weight. Rejection rates above 0.9 were observed at molecular weights between 517.6 and 837.0 g mol^{-1} for the LCM and between 602.9 and 837.0 g mol^{-1} for the LRM. The lower molecular weight cutoff of LCM (517.6 g mol^{-1}) than of LRM (602.9 g mol^{-1}) is attributed to the denser molecular configuration of the LCM, which reduces the membrane porosity. Fitting the pore size distributions to the general logistic function,[81] the dominant pore sizes of the LCM and LRM were estimated as 0.482 and 0.523 nm, respectively (Figure 4L). The OSN data align with the structural features described in "stereoregular self-assembly in the polymers and membranes." The chiral, stereoregularly self-assembled LCM exhibited a denser structure and lower FFVs than the racemic analogue (LRM), resulting in a narrower molecular weight cutoff and a smaller dominant pore size. To further understand the rejection behavior, we obtained the logP values of the solutes (Table S6). The logP is a hydrophobicity measure reflecting the preference of a molecule for organic rather than aqueous environments. Polar and nonpolar (hydrophobic) compounds are characterized by low/negative and high logP values, respectively. Highly polar solutes such as roxithromycin (logP = 1.7) and oleuropein (logP = 0.13) were found in the high-rejection domain (R > 0.9), whereas most of the lowly rejected solutes (R < 0.5) were hydrophobic compounds, including the styrene dimer (logP = 5.29) and estradiol (logP = 4.01). These findings suggest that beyond size exclusion, polarity-governed solute-membrane interactions critically determine the OSN performance.

To further assess the separation performance of the two membranes, we calculated the selectivity figure of merit (SFM; $\beta_{A/B}$) for each solute pair.[82] The binary selectivity increased with increasing molecular size difference between the two solutes. In general, the binary selectivities of the same solute pairs were higher through the LCM membrane (Figure S20A) than through the LRM membrane (Figure S20B). The separation factor was most pronounced between the largest and smallest molecules (the styrene dimer vs. roxithromycin; SFM($\beta_{A/B}$) = 56.3). To further assess the selectivity of the membranes, we analyzed the rejection selectivity against the rejection of the less permeable solute (Figures S20C and S20D). The broader distribution of points in the LCM evaluation than in the LRM evaluation indicates that the LCM better discriminates between solutes with similar properties. To quantify this effect, we calculated the areas enclosed by the data points in the *x*-*y* plane. The substantially larger area coverage of the LCM data (Figure S20C) than of the LRM data (Figure S20D) confirms the higher overall rejection selectivity of the LCM.

The enantioseparation and OSN experiments collectively demonstrate the dual functionality of the chiral membrane (LCM). The incorporation of two distinct stereogenic centers enabled the preferential transport of certain enantiomers (e.g., mandelic acid and phenylalanine). The stereogenic centers established a stereoregular self-assembled membrane with enhanced solvent resistance, broadening its solvent compatibility for OSN applications.

Using a chiral, recyclable polyester, we strategically engineered stereoregular self-assembled membranes with two inherent stereogenic centers for enantiomer separation and OSN. Unlike conventional methods to boost polyester performance, this strategy does not require the blending of different polymer systems. Stereoregular self-assembly harnesses a single polymer whose uniform chain stereochemistry facilitates packing into ordered domains on its own. Stereoregular self-assembly imparts enantioselectivity and increases the degree of molecular ordering, substantially enhancing the chemical, thermal, and mechanical stability of the membrane. The enantioselectivity of the membrane was demonstrated in separation tests of racemic amino acid mixtures. Both the permeate and retentate were analyzed under a range of applied pressures. The membrane was selective for *L*-mandelic acid, achieving an *ee* of 27.12% ± 0.36% in the retentate, and demonstrated water permeance of 12.7 ± 0.3 L m^{-2} h^{-1} bar^{-1}. The observed instances of negative rejection suggested the preferential transport of specific enantiomers. Interestingly, regardless of the rejection direction, the pressure-induced change in rejection value between the two enantiomers was positively correlated with the pressure-induced reduction in enantioselectivity,

Please cite this article in press as: Oldal et al., Stereoregular self-assembly of biobased recyclable polymer membranes for enantioselective nanofiltration, Matter (2026), https://doi.org/10.1016/j.matt.2026.102797

indicating that increasing the pressure impairs chiral separation by minimizing the rejection difference between the enantiomers. The stereoregular packing that governs chiral discrimination also resulted in denser structures favorable for OSN, as evidenced by the effective rejection of solutes down to 517.6 g mol^{-1} and demonstrated methanol permeance of 9.9 ± 0.3 L m^{-2} h^{-1}. The developed membrane with dual functionality—enantioselectivity and broad solvent compatibility—is a promising platform for chiral separation workflows.

METHODS

Materials

DCM (≥99%, GPR RECTAPUR) and ethanol (abs., ≥99.8%, HiPerSolv) were purchased from VWR. Benzyl alcohol and toluene were obtained from Alfa Aesar. Iodine, potassium iodide, and tris(trimethylsilyl)silane were purchased from ACROS Organics. Sodium bicarbonate was purchased from Fisher Chemical. 2,2′-Azobis(2-methylpropionitrile) and tri[N,N-bis(trimethylsilyl)amide] lanthanum(III) were purchased from Sigma-Aldrich. 3-Cyclohexene-1-carboxylic acid and (*R*)-(+)-3-cyclohexenecarboxylic acid were obtained from TCI and Synthonix, respectively.

Polymer synthesis and membrane fabrication

Monomers 6-oxabicyclo[3.2.1]octan-7-one (BiL) and (*R,S*)-6-oxabicyclo[3.2.1]octan-7-one [(*1R,5S*)-BiL] were prepared as detailed in our previous study.[46] The linear polymers were synthesized at a feed ratio of [BiL]:[La-N]:[BnOH] = 600:1:3 in toluene (BiL concentration = 1.28 g mL^{-1} toluene) at room temperature, where La–N and BnOH were added as the catalyst and initiator, respectively. Chiral and racemic polymers were obtained from chiral [(*1R,5S*)-BiL] and racemic BiL monomers, respectively, and their structures were confirmed from ^{1}H and ^{13}C NMR spectra (Figures S2, S3, S4 and S5). The cyclic polymers were synthesized along the same route as the linear ones, but omitting the BnOH initiator. The cyclic polymer production employed only a La–N catalyst for cyclization to form the cyclic polymer. A 3 wt % polymer dope solution was homogenized in DCM by stirring at room temperature, then casted with an Elcometer 4340 film applicator, using a 250-μm thick casting knife. After one minute, they were immersed in an ethanol coagulation bath at room temperature for 24 h.

Characterization methods

The molecular weights of the racemic and chiral polymers were determined using gel permeation chromatography (GPC) on an Agilent 1200 series system. The eluent was chloroform at a flow rate of 1.0 mL min^{-1}. The temperature of the columns and detector was maintained at 40°C. The molar masses were calculated against a reference curve prepared from polystyrene standard samples with known M_w ($<10^2$–1×10^7 Da).

The CD spectra (250–370 nm) at 20°C were recorded using a Jasco J-815 CD spectropolarimeter (Jasco Inc., Japan). Samples of the solution were injected into 10-mm path length quartz cells (Hellma GmbH). The polymer concentration was 10 mg mL^{-1} in chloroform. All spectra were recorded after accumulating 10 runs at a scanning speed of 20 nm min^{-1}. The specific rotations of the enantiomers were measured at 589 nm, using a LAXCO polarimeter model (POL301, Fisher Scientific). The path length was 0.5 dm, and the solutions were prepared at 1 mg mL^{-1} in chloroform. The liquid-phase NMR measurements were recorded on a Bruker AVANCE-III spectrometer operating at a resonance frequency of 500 MHz.

The morphologies of the polyester membranes were investigated using SEM (Magellan SEM, FEI). In preparation for cross-sectional image analysis, the frozen membranes were fractured in liquid nitrogen. Prior to SEM characterization, the membranes were coated with 4-nm iridium, using a sputtering system. AFM (Bruker Dimension ICON) was performed in tapping mode (Acoustic AC) at room temperature. The scanning area was 20 × 20 μm^2, and the scan rate was 0.996 Hz. The results were analyzed using NanoScope Analysis software. The surface roughness of the prepared membranes was measured in terms of the R_q. The R_q results were averaged over three scans.

The water contact angles (WCAs) of the membranes were measured on a Kruss Easydrop instrument by applying the sessile-drop method and ellipse fitting. Prior to measurement, the membranes were adhered with double-sided tape to a glass plate. The final WCA of each sample was calculated as the average of three measurements. XRD data were collected using a Bruker D8 Advance diffractometer within the $2\theta = 5°$–$40°$ range at 0.02° increments and a scanning speed of 2.29° min^{-1}. The freestanding polyester membranes were placed on a zero-background XRD sample holder. WAXS and SAXS measurements were performed on a Xenocs Xeuss 3.0 high-resolution X-ray scattering system, using a Genix3D CuK_α radiation source at wavelength λ = 1.542 Å (50 kV, 60 mA) and a Dectris Eiger2 4M detector. The WAXS and SAXS spectra of all samples were measured for 360 s.

The thermal properties of the polyester membranes were investigated using DSC on a DSC Discovery 250 instrument (TA Instruments) under the following thermal program: (1) initial cycle from 25°C to 120°C, followed by a 5-min isothermal hold to remove any residual solvents and then cooling to 0°C at 5°C min^{-1}; (2) the first heating cycle from 0°C to 280°C at 5°C min^{-1}; (3) a cooling cycle from 280°C to 0°C at 5°C min^{-1}; and (4) the second heating cycle from 0°C to 280°C at 5°C min^{-1}. Thermogravimetric analysis was performed on a Jupiter STA 449 F1 instrument (NETZSCH-Gerätebau) from 30°C to 600°C under an N_2 atmosphere. The temperature ramp rate was 10°C min^{-1}.

The mechanical properties of the polyester membranes were measured on a dynamic mechanical analyzer (DMA) (Q800, TA Instruments). The samples prepared for DMA were rectangular, with dimensions of 20 mm (length), 8 mm (width), and 0.13 mm (thickness). Stress-strain curves of three replicates of each sample were obtained at a force ramp rate of 0.5 N min^{-1}. The Young's moduli were calculated from the linear regions of these curves, and the tensile strengths were obtained from the maximum strain values.

RESOURCE AVAILABILITY

Lead contact

Further information and requests for resources and materials should be directed to and will be fulfilled by the lead contact, Gyorgy Szekely (gyorgy.szekely@kaust.edu.sa).

Materials availability

The details of the material preparation methods can be found in the methods.

Data and code availability

The data that support the findings of this study are available from the corresponding author upon reasonable request.

ACKNOWLEDGMENTS

The research reported in this article was supported by funding from KAUST. We acknowledge the KAUST Supercomputing Laboratory for providing computational resources of the supercomputer Shaheen III. The authors gratefully acknowledge Jumanah Mayet, Feijie Li, and Sanjay Rastogi for their assistance with the GPC measurements, as well as Dominik Renn and Magnus Rueping for their support with the CD analyses. Figure 1 and the graphical abstract were created by Ana Bigio, a scientific illustrator at KAUST. The work performed at Colorado State University was supported by the US Department of Energy, Office of Energy Efficiency and Renewable Energy, Advanced Materials and Manufacturing Technologies Office, and Bioenergy Technologies Office through the BOTTLE Consortium under contract DE-AC36-08GO28308 with the National Laboratory of the Rockies.

AUTHOR CONTRIBUTIONS

D.G.O.: writing – original draft, visualization, validation, methodology, investigation, formal analysis, data curation, conceptualization. R.H.: writing – original draft, visualization, validation, methodology, investigation, formal analysis, data curation, conceptualization. H.V.: writing – original draft, visualization, validation, methodology, investigation, formal analysis, data curation. M.V.P.: methodology, investigation, formal analysis, data curation. U.S.: writing – review and editing, supervision, resources, project administration, methodology. C.S.: writing – review and editing, methodology, investigation. E.Y.-X.C.: writing – review and editing, supervision, resources, project administration, methodology, funding acquisition, conceptualization. G.S.: writing – review and editing, supervision, resources, project administration, methodology, investigation, funding acquisition, conceptualization.

DECLARATION OF INTERESTS

The authors declare no competing interests.

SUPPLEMENTAL INFORMATION

Supplemental information can be found online at https://doi.org/10.1016/j.xcrp.2026.103206.

Received: August 27, 2025
Revised: January 25, 2026
Accepted: March 24, 2026

REFERENCES

1. De Klerck, K., Mangelings, D., and Vander Heyden, Y. (2012). Supercritical fluid chromatography for the enantioseparation of pharmaceuticals. J. Pharm. Biomed. Anal. *69*, 77–92. https://doi.org/10.1016/j.jpba.2012.01.021.
2. Saz, J.M., and Marina, M.L. (2016). Recent advances on the use of cyclodextrins in the chiral analysis of drugs by capillary electrophoresis. J. Chromatogr. A *1467*, 79–94. https://doi.org/10.1016/j.chroma.2016.08.029.
3. Carrão, D.B., Perovani, I.S., de Albuquerque, N.C.P., and de Oliveira, A.R.M. (2020). Enantioseparation of pesticides: A critical review. TrAC Trends Anal. Chem. *122*, 115719. https://doi.org/10.1016/j.trac.2019.115719.
4. Přibylka, A., Švidrnoch, M., Ševčík, J., and Maier, V. (2015). Enantiomeric separation of 1,3-dimethylamylamine by capillary electrophoresis with indirect UV detection using a dual-selector system. Electrophoresis *36*, 2866–2873. https://doi.org/10.1002/elps.201500182.
5. Ng, S.-C., Ong, T.-T., Fu, P., and Ching, C.-B. (2002). Enantiomer separation of flavour and fragrance compounds by liquid chromatography using novel urea-covalent bonded methylated β-cyclodextrins on silica. J. Chromatogr. A *968*, 31–40. https://doi.org/10.1016/S0021-9673(02)00840-3.
6. Bechis, G., Raccary, B., Sarrazin, E., Corbi, E., Peres, C., David, N., Bicchi, C., and Cagliero, C. (2023). Assessing the environmental and overall performance of gas chromatographic analyses. Development of a comprehensive evaluation framework and application to routine chiral analyses of fragrances as a case study. Sustain. Chem. Pharm. *35*, 101217. https://doi.org/10.1016/j.scp.2023.101217.
7. Cheng, Q., Ma, Q., Pei, H., and Mo, Z. (2022). Chiral membranes for enantiomer separation: A comprehensive review. Sep. Purif. Technol. *292*, 121034. https://doi.org/10.1016/j.seppur.2022.121034.
8. Viegas, R., Afonso, C., Crespo, J., and Coelhoso, I. (2007). Modelling of the enantio-selective extraction of propranolol in a biphasic system. Sep. Purif. Technol. *53*, 224–234. https://doi.org/10.1016/j.seppur.2006.07.010.
9. Shen, J., and Okamoto, Y. (2016). Efficient Separation of Enantiomers Using Stereoregular Chiral Polymers. Chem. Rev. *116*, 1094–1138. https://doi.org/10.1021/acs.chemrev.5b00317.
10. Gänsch, J., Huskova, N., Kerst, K., Temmel, E., Lorenz, H., Mangold, M., Janiga, G., and Seidel-Morgenstern, A. (2021). Continuous enantioselective crystallization of chiral compounds in coupled fluidized beds. Chem. Eng. J. *422*, 129627. https://doi.org/10.1016/j.cej.2021.129627.
11. Cui, X., Ding, Q., Shan, R.N., He, C.H., and Wu, K.J. (2019). Enantioseparation of flurbiprofen enantiomers using chiral ionic liquids by liquid-liquid extraction. Chirality *31*, 457–467. https://doi.org/10.1002/chir.23071.
12. Lorenz, H., and Seidel-Morgenstern, A. (2014). Processes To Separate Enantiomers. Angew. Chem. Int. Ed. Engl. *53*, 1218–1250. https://doi.org/10.1002/anie.201302823.
13. Yan, Y.-X., Zhang, Y., Chen, Y., and Liu, Y. (2020). Cyclodextrin-Based Supramolecular Hydrogel as a Selective Chiral Adsorption/Separation Platform for Tryptophan Enantiomers. ACS Appl. Polym. Mater. *2*, 5641–5645. https://doi.org/10.1021/acsapm.0c00958.
14. Cheng, Q., Ma, Q., Pei, H., He, S., Wang, R., Guo, R., Liu, N., and Mo, Z. (2023). Enantioseparation Membranes: Research Status, Challenges, and Trends. Small *19*, e2300376. https://doi.org/10.1002/smll.202300376.
15. Vedovello, P., Marcio Paranhos, C., Fernandes, C., and Elizabeth Tiritan, M. (2022). Chiral polymeric membranes: Recent applications and trends. Sep. Purif. Technol. *280*, 119800. https://doi.org/10.1016/j.seppur.2021.119800.
16. Kang, X., Stephens, E.R., Spector-Watts, B.M., Li, Z., Liu, Y., Liu, L., and Cui, Y. (2022). Challenges and opportunities for chiral covalent organic frameworks. Chem. Sci. *13*, 9811–9832. https://doi.org/10.1039/D2SC02436E.
17. Ingole, P.G., and Ingole, N.P. (2014). Methods for separation of organic and pharmaceutical compounds by different polymer materials. Korean J. Chem. Eng. *31*, 2109–2123. https://doi.org/10.1007/s11814-014-0284-z.
18. Keurentjes, J.T.F., Nabuurs, L.J.W.M., and Vegter, E.A. (1996). Liquid membrane technology for the separation of racemic mixtures. J. Memb. Sci. *113*, 351–360. https://doi.org/10.1016/0376-7388(95)00176-X.
19. Xie, R., Chu, L.-Y., and Deng, J.-G. (2008). Membranes and membrane processes for chiral resolution. Chem. Soc. Rev. *37*, 1243–1263. https://doi.org/10.1039/b713350b.
20. Qiu, X., Ke, J., Chen, W., Liu, H., Bai, X., Ji, Y., and Chen, J. (2022). β-Cyclodextrin-ionic liquid functionalized chiral composite membrane for enantioseparation of drugs and molecular simulation. J. Memb. Sci. *660*, 120870. https://doi.org/10.1016/j.memsci.2022.120870.

21. Ong, C.S., Oor, J.Z., Tan, S.J., and Chew, J.W. (2022). Enantiomeric Separation of Racemic Mixtures Using Chiral-Selective and Organic-Solvent-Resistant Thin-Film Composite Membranes. ACS Appl. Mater. Interfaces *14*, 10875–10885. https://doi.org/10.1021/acsami.1c25175.

22. Liu, J., Yuan, W., Li, C., Cheng, M., Su, Y., Xu, L., Chu, T., and Hou, S. (2021). L-Cysteine-Modified Graphene Oxide-Based Membrane for Chiral Selective Separation. ACS Appl. Mater. Interfaces *13*, 49215–49223. https://doi.org/10.1021/acsami.1c14900.

23. Nikam, S.B., and SK, A. (2020). Enantioselective Separation Using Chiral Amino Acid Functionalized Polyfluorene Coated on Mesoporous Anodic Aluminum Oxide Membranes. Anal. Chem. *92*, 6850–6857. https://doi.org/10.1021/acs.analchem.9b04699.

24. Matsuoka, Y., Kanda, N., Lee, Y.M., and Higuchi, A. (2006). Chiral separation of phenylalanine in ultrafiltration through DNA-immobilized chitosan membranes. J. Memb. Sci. *280*, 116–123. https://doi.org/10.1016/j.memsci.2006.01.013.

25. Liu, J., Chu, T., Cheng, M., Su, Y., Zou, G., and Hou, S. (2023). Bovine serum albumin functional graphene oxide membrane for effective chiral separation. J. Memb. Sci. *668*, 121198. https://doi.org/10.1016/j.memsci.2022.121198.

26. Demirel, N., Bulut, Y., and Hoşgören, H. (2004). Enantioselective transport and liquid-liquid extraction of amino acids as their potassium and sodium salts by optically active diaza-18-crown-6 ethers. Chirality *16*, 347–350. https://doi.org/10.1002/chir.20046.

27. Wang, W., Dong, X., Nan, J., Jin, W., Hu, Z., Chen, Y., and Jiang, J. (2012). A homochiral metal–organic framework membrane for enantioselective separation. Chem. Commun. *48*, 7022–7024. https://doi.org/10.1039/c2cc32595k.

28. Lu, Y., Zhang, H., Chan, J.Y., Ou, R., Zhu, H., Forsyth, M., Marijanovic, E.M., Doherty, C.M., Marriott, P.J., Holl, M.M.B., and Wang, H. (2019). Homochiral MOF–Polymer Mixed Matrix Membranes for Efficient Separation of Chiral Molecules. Angew. Chemie *131*, 17084–17091. https://doi.org/10.1002/ange.201910408.

29. Wang, Z., Zhang, S., Chen, Y., Zhang, Z., and Ma, S. (2020). Covalent organic frameworks for separation applications. Chem. Soc. Rev. *49*, 708–735. https://doi.org/10.1039/C9CS00827F.

30. Zhang, S., Zhou, J., and Li, H. (2022). Chiral Covalent Organic Framework Packed Nanochannel Membrane for Enantioseparation. Angew. Chem. Int. Ed. Engl. *61*, e202204012. https://doi.org/10.1002/anie.202204012.

31. Qiu, X., Chen, W., Chen, Y., Ke, J., Ji, Y., and Chen, J. (2023). Separation of chiral drugs through dual chiral ionic liquid functionalized composite membrane and study on chiral recognition mechanism. J. Memb. Sci. *687*, 122087. https://doi.org/10.1016/j.memsci.2023.122087.

32. Wang, F., Pizzi, D., Lu, Y., He, K., Thurecht, K.J., Hill, M.R., Marriott, P.J., Banaszak Holl, M.M., Kempe, K., and Wang, H. (2023). A Homochiral Poly(2-oxazoline)-based Membrane for Efficient Enantioselective Separation. Angew. Chem. Int. Ed. Engl. *62*, e202212139. https://doi.org/10.1002/anie.202212139.

33. Zhang, Q.P., Wang, Z., Zhang, Z.W., Zhai, T.L., Chen, J.J., Ma, H., Tan, B., and Zhang, C. (2021). Triptycene-based Chiral Porous Polyimides for Enantioselective Membrane Separation. Angew. Chem. Int. Ed. Engl. *60*, 12781–12785. https://doi.org/10.1002/anie.202102350.

34. Weng, X., Baez, J.E., Khiterer, M., Hoe, M.Y., Bao, Z., and Shea, K.J. (2015). Chiral Polymers of Intrinsic Microporosity: Selective Membrane Permeation of Enantiomers. Angew. Chem. Int. Ed. Engl. *54*, 11214–11218. https://doi.org/10.1002/anie.201504934.

35. Zhao, H., Shao, L., and Chen, J.F. (2010). High-gravity process intensification technology and application. Chem. Eng. J. *156*, 588–593. https://doi.org/10.1016/j.cej.2009.04.053.

36. Xiong, W.-W., Wang, W.-F., Zhao, L., Song, Q., and Yuan, L.-M. (2009). Chiral separation of (R,S)-2-phenyl-1-propanol through glutaraldehyde-crosslinked chitosan membranes. J. Memb. Sci. *328*, 268–272. https://doi.org/10.1016/j.memsci.2008.12.019.

37. Yuan, L.M., Ma, W., Xu, M., Zhao, H.L., Li, Y.Y., Wang, R.L., Duan, A.H., Ai, P., and Chen, X.X. (2017). Optical resolution and mechanism using enantioselective cellulose, sodium alginate and hydroxypropyl-β-cyclodextrin membranes. Chirality *29*, 315–324. https://doi.org/10.1002/chir.22693.

38. Flores-López, L.Z., Caloca, J., Rogel-Hernández, E., and Espinoza-Gomez, H. (2014). Development of an enantioselective membrane from cellulose acetate propionate/cellulose acetate, for the separation of trans-stilbene oxide. Cellulose *21*, 1987–1995. https://doi.org/10.1007/s10570-014-0252-0.

39. Galiano, F., Briceño, K., Marino, T., Molino, A., Christensen, K.V., and Figoli, A. (2018). Advances in biopolymer-based membrane preparation and applications. J. Memb. Sci. *564*, 562–586. https://doi.org/10.1016/j.memsci.2018.07.059.

40. Ke, J., Yang, K., Bai, X., Luo, H., Ji, Y., and Chen, J. (2021). A novel chiral polyester composite membrane: Preparation, enantioseparation of chiral drugs and molecular modeling evaluation. Sep. Purif. Technol. *255*, 117717. https://doi.org/10.1016/j.seppur.2020.117717.

41. Lu, Y., Zhang, H., Liu, S., Wang, F., Banaszak Holl, M.M., Marriott, P.J., and Wang, H. (2022). Precise sieving of chiral molecules by a crosslinked cyclodextrin-cellulose nanofiber composite membrane. J. Memb. Sci. *663*, 121016. https://doi.org/10.1016/j.memsci.2022.121016.

42. Szweda, R. (2023). Sequence- and stereo-defined macromolecules: Properties and emerging functionalities. Prog. Polym. Sci. *145*, 101737. https://doi.org/10.1016/j.progpolymsci.2023.101737.

43. Tang, X., Westlie, A.H., Watson, E.M., and Chen, E.Y.-X. (2019). Stereosequenced crystalline polyhydroxyalkanoates from diastereomeric monomer mixtures. Science *366*, 754–758. https://doi.org/10.1126/science.aax8466.

44. Worch, J.C., Prydderch, H., Jimaja, S., Bexis, P., Becker, M.L., and Dove, A.P. (2019). Stereochemical enhancement of polymer properties. Nat. Rev. Chem *3*, 514–535. https://doi.org/10.1038/s41570-019-0117-z.

45. Childers, M.I., Longo, J.M., Van Zee, N.J., LaPointe, A.M., and Coates, G.W. (2014). Stereoselective Epoxide Polymerization and Copolymerization. Chem. Rev. *114*, 8129–8152. https://doi.org/10.1021/cr400725x.

46. Shi, C., Li, Z.-C., Caporaso, L., Cavallo, L., Falivene, L., and Chen, E.Y.-X. (2021). Hybrid monomer design for unifying conflicting polymerizability, recyclability, and performance properties. Chem *7*, 670–685. https://doi.org/10.1016/j.chempr.2021.02.003.

47. Hardian, R., Cywar, R.M., Chen, E.Y.-X., and Szekely, G. (2022). Sustainable nanofiltration membranes based on biosourced fully recyclable polyesters and green solvents. J. Membr. Sci. Lett. *2*, 100016. https://doi.org/10.1016/j.memlet.2022.100016.

48. Hardian, R., Ghaffar, A., Shi, C., Chen, E.Y.-X., and Szekely, G. (2024). Chemically recyclable nanofiltration membranes fabricated from two circular polymer classes of the same monomer origin. J. Membr. Sci. Lett. *4*, 100067. https://doi.org/10.1016/j.memlet.2024.100067.

49. Bozell, J.J., and Petersen, G.R. (2010). Technology development for the production of biobased products from biorefinery carbohydrates—the US Department of Energy's "Top 10" revisited. Green Chem. *12*, 539. https://doi.org/10.1039/b922014c.

50. Kaluzynski, K., Pretula, J., Lewinski, P., Kaźmierski, S., and Penczek, S. (2022). Synthesis and Properties of Functionalized Poly(ε-caprolactone); Chain Polymerization Followed by Polycondensation in One Pot with Initiator and Catalyst in One Molecule. Synthesis and Molecular Structures. Macromolecules *55*, 2210–2221. https://doi.org/10.1021/acs.macromol.1c02325.

51. Thomas, S.M., DiCosimo, R., and Nagarajan, V. (2002). Biocatalysis: applications and potentials for the chemical industry. Trends Biotechnol. *20*, 238–242. https://doi.org/10.1016/S0167-7799(02)01935-2.

52. Rodger, A. (2013). Circular Dichroism and Chirality. In Encyclopedia of Biophysics (Springer Berlin Heidelberg), pp. 311–313. https://doi.org/10.1007/978-3-642-16712-6_646.

53. Berova, N., Di Bari, L., and Pescitelli, G. (2007). Application of electronic circular dichroism in configurational and conformational analysis of organic compounds. Chem. Soc. Rev. *36*, 914–931. https://doi.org/10.1039/b515476f.

54. Okada, Y., Yamamoto, C., Kamigaito, M., Gao, Y., Shen, J., and Okamoto, Y. (2016). Enantioseparation Using Cellulose Tris(3,5-dimethylphenylcarbamate) as Chiral Stationary Phase for HPLC: Influence of Molecular Weight of Cellulose. Molecules *21*, 1484. https://doi.org/10.3390/molecules21111484.

55. Zhang, G.-H., Xi, J.-B., Chen, W., and Bai, Z.-W. (2020). Comparison in enantioseparation performance of chiral stationary phases prepared from chitosans of different sources and molecular weights. J. Chromatogr. A *1621*, 461029. https://doi.org/10.1016/j.chroma.2020.461029.

56. Mei, X.-M., Chen, W., and Bai, Z.-W. (2017). Enantioseparation characteristics of the chiral stationary phases based on natural and regenerated chitins. J. Sep. Sci. *40*, 1710–1717. https://doi.org/10.1002/jssc.201700032.

57. Regenspurg, J.A., Martins Costa, A.F., Achterhuis, I., and de Vos, W.M. (2022). Influence of Molecular Weight on the Performance of Polyelectrolyte Multilayer Nanofiltration Membranes. ACS Appl. Polym. Mater. *4*, 2962–2971. https://doi.org/10.1021/acsapm.1c00826.

58. Popowski, Y., Lu, Y., Coates, G.W., and Tolman, W.B. (2022). Stereocomplexation of Stereoregular Aliphatic Polyesters: Change from Amorphous to Semicrystalline Polymers with Single Stereocenter Inversion. J. Am. Chem. Soc. *144*, 8362–8370. https://doi.org/10.1021/jacs.2c02981.

59. Flory, P.J. (1941). Thermodynamics of High Polymer Solutions. J. Chem. Phys. *9*, 660. https://doi.org/10.1063/1.1750971.

60. Huggins, M.L. (1941). Solutions of Long Chain Compounds. J. Chem. Phys. *9*, 440. https://doi.org/10.1063/1.1750930.

61. Meaurio, E., Hernandez-Montero, N., Zuza, E., and Sarasua, J. (2014). Miscible Blends Based on Biodegradable Polymers. In Characterization of Polymer Blends (Wiley)), pp. 7–92. https://doi.org/10.1002/9783527645602.ch02.

62. Wan, Z.-Q., Longo, J.M., Liang, L.-X., Chen, H.-Y., Hou, G.-J., Yang, S., Zhang, W.-P., Coates, G.W., and Lu, X.-B. (2019). Comprehensive Understanding of Polyester Stereocomplexation. J. Am. Chem. Soc. *141*, 14780–14787. https://doi.org/10.1021/jacs.9b07058.

63. Cui, J., Yang, S.-G., Zhang, R., Cao, Y., Wang, Y., Zeng, X., Liu, F., and Ungar, G. (2023). Continuous Spectrum of Morphologies and Phase Behavior across the Contact Zone from Poly(l-lactide) to Poly(d-lactide): Stereocomplex, Homocrystal, and Between. Macromolecules *56*, 8754–8766. https://doi.org/10.1021/acs.macromol.3c01815.

64. Bauer, P.S., Amenitsch, H., Baumgartner, B., Köberl, G., Rentenberger, C., and Winkler, P.M. (2019). In-situ aerosol nanoparticle characterization by small angle X-ray scattering at ultra-low volume fraction. Nat. Commun. *10*, 1122. https://doi.org/10.1038/s41467-019-09066-4.

65. Zhang, X., Kyriakos, K., Rikkou-Kalourkoti, M., Kitiri, E.N., Patrickios, C.S., and Papadakis, C.M. (2016). Amphiphilic single and double networks: a small-angle X-ray scattering investigation. Colloid Polym. Sci. *294*, 1027–1036. https://doi.org/10.1007/s00396-016-3856-0.

66. Banks, A., Qin, S., Weiss, K.L., Stanley, C.B., and Zhou, H.-X. (2018). Intrinsically Disordered Protein Exhibits Both Compaction and Expansion under Macromolecular Crowding. Biophys. J. *114*, 1067–1079. https://doi.org/10.1016/j.bpj.2018.01.011.

67. Parker, C.R., Zhang, Z., Quinn, E.C., Reilly, L.T., and Chen, E.Y.-X. (2025). Stereoregular cyclic poly(3-hydroxybutyrate) enabled by catalyst-controlled tacticity and topology. Polym. Chem. *16*, 1713–1722. https://doi.org/10.1039/D4PY01304B.

68. He, L., Jiang, Y., Wei, J., Zhang, Z., Hong, T., Ren, Z., Huang, J., Huang, F., Stang, P.J., and Li, S. (2024). Highly robust supramolecular polymer networks crosslinked by a tiny amount of metallacycles. Nat. Commun. *15*, 3050. https://doi.org/10.1038/s41467-024-47333-1.

69. Berthod, A. (2006). Chiral Recognition Mechanisms. Anal. Chem. *78*, 2093–2099. https://doi.org/10.1021/ac0693823.

70. Wang, Y., Wu, N., Wang, Y., Ma, H., Zhang, J., Xu, L., Albolkany, M.K., and Liu, B. (2019). Graphite phase carbon nitride based membrane for selective permeation. Nat. Commun. *10*, 2500. https://doi.org/10.1038/s41467-019-10381-z.

71. Liu, T., Li, Z., Wang, J., Chen, J., Guan, M., and Qiu, H. (2021). Solid membranes for chiral separation: A review. Chem. Eng. J. *410*, 128247. https://doi.org/10.1016/j.cej.2020.128247.

72. Gumí, T., Ferreira, Q., Viegas, R.M.C., Crespo, J.G., Coelhoso, I.M., and Palet, C. (2005). Enantioselective Separation of Propranolol by Chiral Activated Membranes. Sep. Sci. Technol. *40*, 773–789. https://doi.org/10.1081/SS-200044732.

73. Gaálová, J., Michel, M., Bourassi, M., Ladewig, B.P., Kasal, P., Jindřich, J., and Izák, P. (2021). Nafion membranes modified by cationic cyclodextrin derivatives for enantioselective separation. Sep. Purif. Technol. *266*, 118538. https://doi.org/10.1016/j.seppur.2021.118538.

74. Zhou, Z., He, L., Mao, Y., Chai, W., and Ren, Z. (2017). Green preparation and selective permeation of d-Tryptophan imprinted composite membrane for racemic tryptophan. Chem. Eng. J. *310*, 63–71. https://doi.org/10.1016/j.cej.2016.10.070.

75. Berthod, A. (2010). Chiral Recognition Mechanisms in Enantiomers Separations: A General View. In Chiral Recognition in Separation Methods (Springer Berlin Heidelberg), pp. 1–32. https://doi.org/10.1007/978-3-642-12445-7_1.

76. Wijmans, J.G., and Baker, R.W. (1995). The solution-diffusion model: a review. J. Memb. Sci. *107*, 1–21. https://doi.org/10.1016/0376-7388(95)00102-I.

77. Volkov, A., Yushkin, A., Kachula, Y., Khotimsky, V., and Volkov, V. (2014). Application of negative retention in organic solvent nanofiltration for solutes fractionation. Sep. Purif. Technol. *124*, 43–48. https://doi.org/10.1016/j.seppur.2013.12.044.

78. Liu, W., Li, R., Liu, J., Ma, X., Xiao, Y., and Wang, Y. (2021). Nacre-like ultra-robust supramolecular-functionalized graphene oxide membrane for bifunctional separation. Carbon N. Y. *184*, 618–626. https://doi.org/10.1016/j.carbon.2021.08.068.

79. Liu, J., Zou, G., and Hou, S. (2023). Chiral gold nanoparticles/graphene oxide membranes with ultrahigh and stable permeance for sieving and enantioseparation. Chem. Eng. J. *467*, 143366. https://doi.org/10.1016/j.cej.2023.143366.

80. Karan, S., Jiang, Z., and Livingston, A.G. (2015). Sub–10 nm polyamide nanofilms with ultrafast solvent transport for molecular separation. Science *348*, 1347–1351. https://doi.org/10.1126/science.aaa5058.

81. Martinez, K.M., Hardian, R., Ignacz, G., and Szekely, G. (2025). Automating the determination of pore size distribution in liquid separation membranes via solute retention experiments. J. Memb. Sci. *726*, 124015. https://doi.org/10.1016/j.memsci.2025.124015.

82. Alhazmi, B., Ignacz, G., Di Vincenzo, M., Hedhili, M.N., Szekely, G., and Nunes, S.P. (2024). Ultraselective Macrocycle Membranes for Pharmaceutical Ingredients Separation in Organic Solvents. Nat. Commun. *15*, 7151. https://doi.org/10.1038/s41467-024-51548-7.